

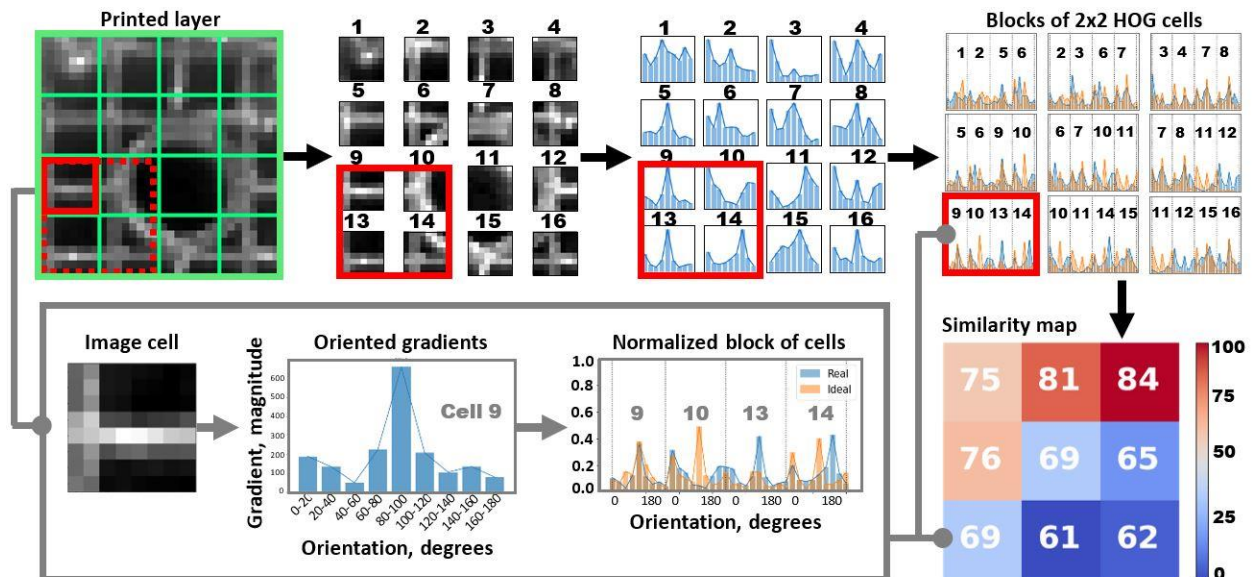
# Towards Smart Monitored AM: Open Source in-Situ Layer-wise 3D Printing Image Anomaly Detection Using Histograms of Oriented Gradients and a Physics-Based Rendering Engine

Aliaksei Petsiuk<sup>1</sup> and Joshua M. Pearce<sup>2\*</sup>

1. Department of Electrical & Computer Engineering, Michigan Technological University, Houghton, MI, USA
2. Department of Electrical & Computer Engineering, Western University, ON, Canada

[apetsiuk@mtu.edu](mailto:apetsiuk@mtu.edu), \* [joshua.pearce@uwo.ca](mailto:joshua.pearce@uwo.ca)

## Graphical abstract



## Highlights

- In-situ layer-wise 3D printing anomaly detection is based on reference images.
- G-code-based synthetic references are created in a physics rendering engine.
- The system analyzes the similarity of local histograms of oriented gradients.
- Failure detection resolution is 5-10% of the entire observation area.
- The method allows noticing critical errors in the early stages of their occurrence.

## Abstract

This study presents an open source method for detecting 3D printing anomalies by comparing images of printed layers from a stationary monocular camera with G-code-based reference images of an ideal process generated with Blender, a physics rendering engine. Recognition of visual deviations was accomplished by analyzing the similarity of histograms of oriented gradients (HOG) of local image areas. The developed technique requires preliminary modeling of the

working environment to achieve the best match for orientation, color rendering, lighting, and other parameters of the printed part. The output of the algorithm is a level of mismatch between printed and synthetic reference layers. Twelve similarity and distance measures were implemented and compared for their effectiveness at detecting 3D printing errors on six different representative failure types (local infill defects, presence of a foreign body in the layer, spaghetti problem, separation and shift of the printing part from the working surface, defects in thin walls, and layer shift) and their control error-free print images. The results show that although Kendall's tau, Jaccard, and Sorensen similarities are the most sensitive, Pearson's r, Spearman's rho, cosine, and Dice similarities produce the more reliable results. This open source method allows the program to notice critical errors in the early stages of their occurrence and either pause manufacturing processes for further investigation by an operator or in the future AI-controlled automatic error correction. The implementation of this novel method does not require preliminary data for training, and the greatest efficiency can be achieved with the mass production of parts by either additive or subtractive manufacturing of the same geometric shape. It can be concluded this open source method is a promising means of enabling smart distributed recycling for additive manufacturing using complex feedstocks as well as other challenging manufacturing environments.

**Keywords:** 3D modeling, 3D printing, additive manufacturing, anomaly detection, Blender, feature descriptor, HOG, similarity measure, synthetic images

## 1. Introduction

Over the past decades, additive manufacturing (AM) has become a widespread technology that has found application in various fields of science and technology. AM allows the fabrication of high-performance components with complex geometries and continues to attract research interest. Extrusion-based 3D printing, democratized with the open source release of the self-replicating rapid prototyper (RepRap) [1-3], dominates the technology arena due to its low cost [4], availability of components, and a wide variety of printing materials [5,6] including waste plastics [7-10]. Despite its affordability and relative ease of use, however, this technology is not free from fabrication failures, which reduces economic impact [11,12], environmental merits [13], and limits the prospects for industrialization [14,15].

According to a recent comprehensive state-of-the-art review of monitoring techniques for material extrusion AM [16], the number of publications in the field of anomaly analysis grows steadily as this is a major impediment to widespread deployment. The vast majority of research has been conducted in the fused filament fabrication (FFF) domain [16]. This phenomenon can be explained by the fact that FFF technology dominates the 3D printing market for printers in use [17].

Analysis of extrusion-based AM processes can consist of examining parameters such as temperature [18,19], vibration [20,21], acoustic emissions [22,23], electrical characteristics [24,25], and others [26-29]. The main source of information, however, remains 2D and 3D image data obtained from single or multiple camera systems [16]. Since 3D printed parts are mostly

fabricated in layers, most of the developed failure detection methods analyze manufacturing processes after a certain number of layers have been printed. Nuchitprasitchai et al. [30], Johnson et al. [31], and Hurd [32] proposed the concepts of failure analysis based on comparison with Standard Tessellation Language (STL) files. Jeong et al. [33] and Wasserfall et al. [34] employed information obtained from G-code files of printing parts. Ceruti et al. [35] utilized data from computer-aided design (CAD) files. Researchers also use comparison with reference data [36,37] or ideal printing processes [38,39]. Malik et al. [40] presented a 3D reconstruction-based scanning method for real-time monitoring of AM processes.

Having a way to automatically detect critical errors will significantly reduce material waste and time spent on failed prints. In order to reach this goal, this study reports on a developed monocular system for the analysis of plastic FFF processes that monitors contour deviations and infill distortions for each layer. This work expands on previous developments of the authors [41] by using an open-source physics rendering engine to generate G-code-based synthetic reference images for each printing stage. With certain rendering parameters, a synthetic image can represent a real captured layer under ideal printing conditions. It is hypothesized that further comparative texture analysis based on image processing techniques can reveal the location and the degree of structural deviations. To this end a material extrusion-based 3D printer was monitored with a stationary monocular camera. Synthetic reference images for the setup were created with open-source and free Blender. Images were compared based on the similarity degree of the feature descriptors, represented by histograms of oriented gradients. Twelve similarity and distance measures were implemented and compared for their effectiveness at detecting 3D printing errors on six different representative failure types (local infill defects, presence of a foreign body in the layer, spaghetti problem, separation and shift of the printing part from the working surface, defects in thin walls, and layer shift) and their control error-free print images. The sensitivities of the measures are quantified and the results are discussed in the context of creating artificial intelligence (AI)-guided smart additive and subtractive manufacturing devices.

## **2. Method**

### **2.1. Experimental apparatus**

For experimental tests, an open source delta-style FFF-based 3D printer [42] was used, which represents a derivative of the self-replicating rapid prototype (RepRap) printer [1-3]. The device operates in Cartesian coordinates under the control of a RepRap Arduino Mega Polulu Shield (RAMPS) system [43]. It has a cylindrical volume of  $\text{Ø}240 \times 250$  mm and an extruder with a 0.4 mm nozzle diameter. The main feedstock material is 1.75 mm polylactic acid (PLA) plastic filament.

A stationary monocular camera is mounted on a tripod near the printing bed at an angle of  $\sim 45$  degrees. The camera is based on a 2-megapixel 1/2.9-inch Sony IMX322 CMOS sensor [44] and has manual focus and aperture control. As shown in Figure 1, the four white dots on the printing surface are visual markers for the camera position and orientation determination. The markers indicate the active 90x90 mm observation area with the origin in the center of the square.

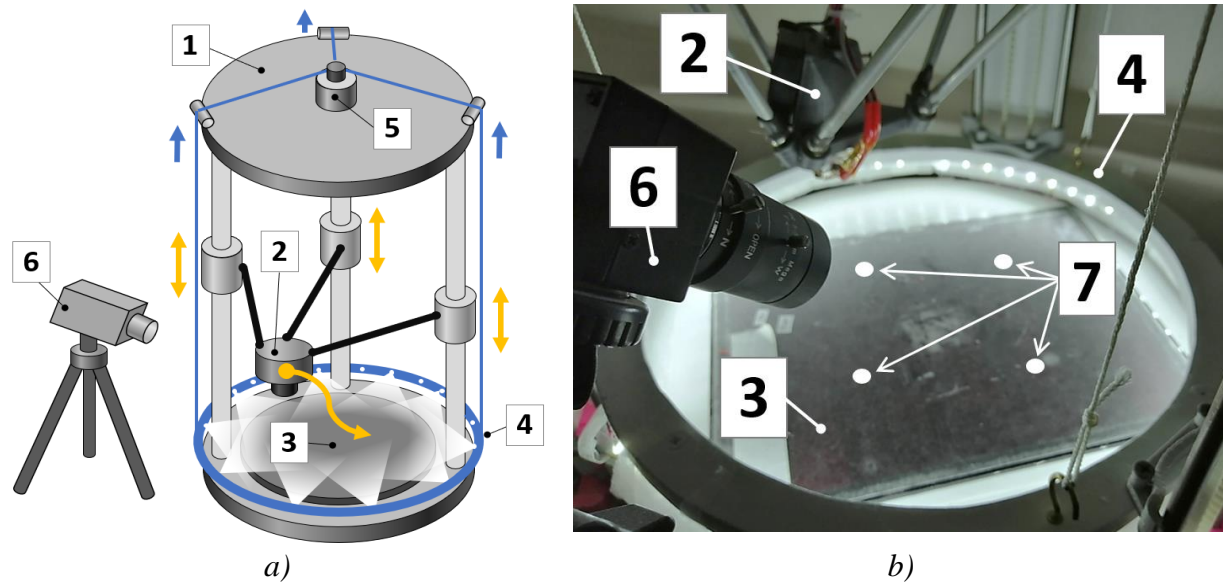


**Figure 1. Experimental apparatus: a) 3D printer schematic, b) printing area. 1 – 3D printer, 2 – extruder, 3 – printing bed, 4 – movable circular lighting platform, 5 – lighting platform drive system, 6 – camera, 7 – visual markers.**

A movable circular lighting platform [41], controlled through G-code, is located above the working surface. The light frame consists of 56 light-emitting diodes with a glowing temperature of 6000K and a total power of 18 watts. The stepper motor driving the mechanical structure is located on top of the printer and is connected to the RAMPS controller as an additional extruder.

**Table 1. Interlayer G-code commands**

G-code command	Description
M400	Wait for moves to finish
G91	Switch to relative coordinates
G1 E-20 F1000	Retract the filament 10 mm before lifting the nozzle
G1 Z80	Move the nozzle 80 mm up
G1 X20 Y20	Move the nozzle 20 mm aside
T1	Set the active extruder to 1 (lighting platform)
G1 E-0.25 F600	Move the lighting platform one layer height up
M400	Wait for moves to finish
M42 P57 S200	Indicator ON (optional)
<b>Create layer snapshot</b>	
G1 X-20 Y-20	Move the nozzle 20 mm back
G1 Z-80	Move the nozzle 80 mm down
G4 P500	Wait 500ms for the nozzle vibration to stabilize
T0	Set the active extruder to 0 (extruder nozzle)
G90	Switch to absolute coordinates
M42 P57 S0	Indicator OFF (optional)

Table 1 shows a set of G-code commands that are placed after the printing instructions for each layer. This pauses the fabrication process, moves the extruder out of the video surveillance area,

and raises the lighting platform to a height equal to the thickness of the printed layer. Thus, the active print area is evenly lit around the perimeter, regardless of the current layer and the working level of the extruder nozzle. This allows capturing 2D images of each completed layer with uniform illumination and applying unified image processing techniques to each image frame.

## 2.2. Creation of synthetic reference images

Synthetic reference images represent the ideal 3D printed model fabricated in optimal conditions. The open-source and free Blender [45] software was used to create images for each layer during the printing process. It is a multifunctional software environment for 3D graphics. The set of Blender tools includes 3D modeling, lighting and animation control, texture editing, and photorealistic rendering. There is also a Python scripting interface for customizing and automating the entire production pipeline.

Figure 2 depicts a virtual model of the key parts of the Delta printer in use.

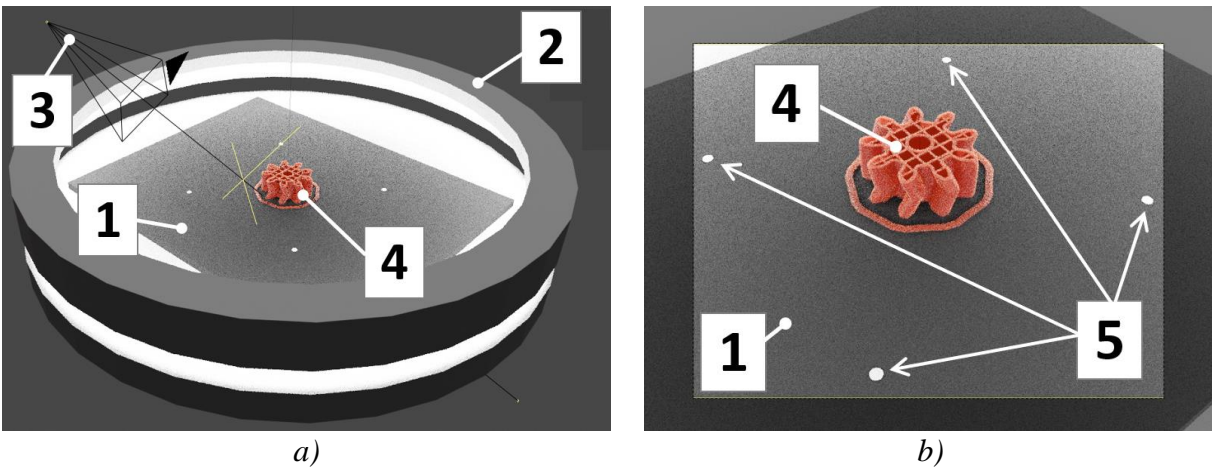


**Figure 2. Virtual workspace: a) main elements of the Delta printer modeled in Blender, b) virtual camera view area. 1 – printing bed, 2 – movable lighting platform, 3 – camera, 4 – rendered G-code, 5 – visual markers.**

Previous research has repeatedly shown that Blender can be used as a reliable and flexible physics simulating environment for solving scientific and engineering problems. Kent [46] utilized Blender to visualize astronomical data, Gschwandtner et al. [47] and Romulo Fernandes et al. [48] performed range sensor testing and radar simulations, respectively. Fleischlen and Wehinger [49] performed particle-resolved computational fluid dynamics modelling for chemical industry, Ilba [50] estimated solar irradiation on buildings, Rohe [51] created an optical test simulator, and, finally, Reitmann et al. [52] developed an add-on to generate semantically labeled depth-sensing data in Blender.

To create realistic images of the ideal printing process, the main components of the Delta printer have been modeled while maintaining relative proportions (Figure 2). Based on the authors' experiments and experience of professional 3D computer graphics communities [53,54], a shader graph was developed for the procedural generation of realistic plastic textures (Figure 3).

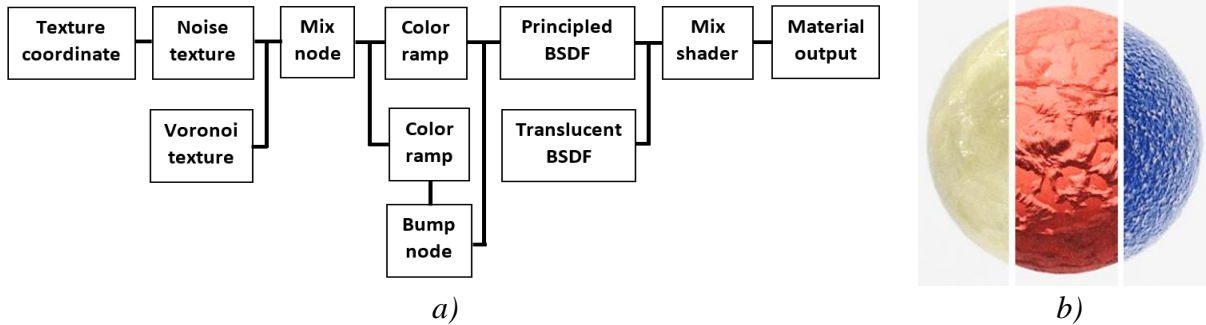


**Figure 3. Shader graph for procedural texture generation: a) shader nodes, b) procedural texture samples**

The main nodes are the Principled and Translucent Bidirectional Scattering Distribution Functions (BSDFs). The Principled BSDF shader includes multiple material properties (roughness, reflection, transmission, sheen, etc.) as layers to create a wide variety of materials, and the Translucent BSDF adds Lambertian diffuse transmission [55]. The texture shaders, in turn, add natural surface irregularities. Changing the parameters of the nodes allows maximizing similarity with the real printed parts. The given graph (Figure 3, a) was used to visualize the photorealistic textures of the printed parts. In addition, a single material node with emissive characteristics was used to model the lighting frame.

To print a specific product, it is necessary to have its representation in the STL format, which describes the 3D object as a list of unit normals and vertices of its tessellated surface. During the process of slicing, the STL file is converted into G-code—a set of step-by-step trajectory coordinates for the printer extruder. Several G-code exporters [56-59] were used as references in this work.

An open source software toolchain has the G-code of the printing part to be loaded into the Blender programming interface and parsed layer by layer, where the extruder path is converted into a set of curves with an adjustable thickness parameter and preset material settings [60]. Therefore, each cross-section of the object can be represented as a G-code-based extruder path and an STL-based mask of the filled regions (Figure 4).

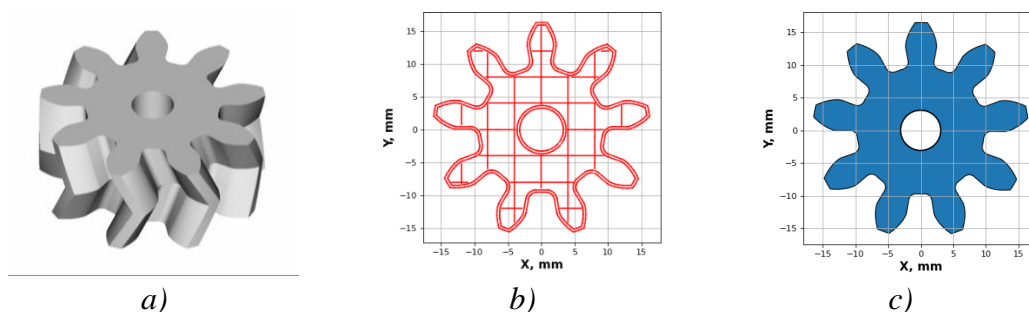


**Figure 4. Printing object: a) STL file of the whole part, b) G-code of a layer cross-section, c) STL-based layer cross-section mask**

In the programmed 3D printing animation, a new printing layer is added with each consecutive frame, and the lighting platform is raised to the corresponding height until the "virtual print" is

complete. Each frame is rendered with Blender Cycles [61], a physics-based path tracer, and saved as a separate image—a "quality standard" for comparison with the actual camera image of the printed layer.

### 2.3. Comparison of the printed layer with the reference image

The camera is positioned at an angle to the working area, which, however, makes it possible to visually rotate the active print surface (Figure 5) using a perspective projection (1) [62,63].

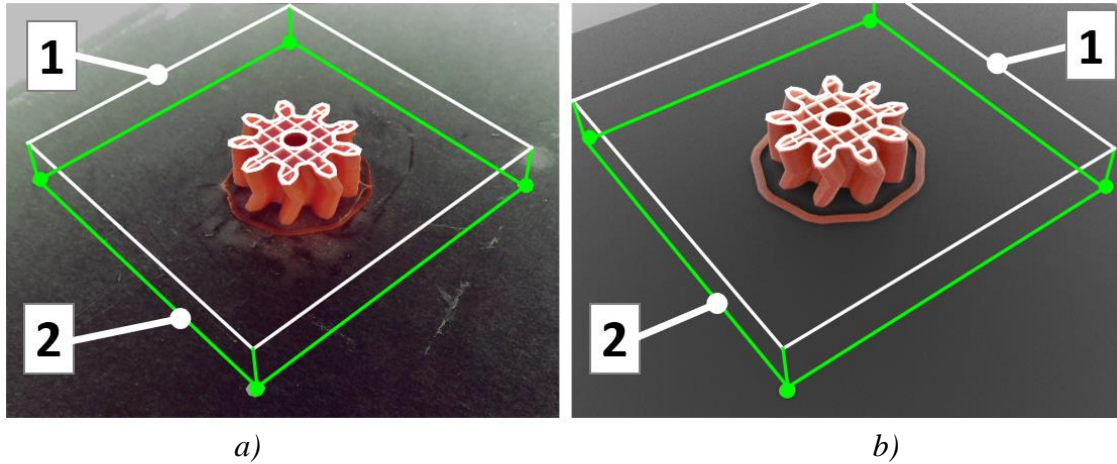


**Figure 5. Spatial position of the active printing area: a) real image, b) rendered image. 1 – active printing plane, 2 – print surface plane.**

Thus, regardless of the actual position and orientation of the camera, the virtual top views are used to analyze the AM process as if the camera was mounted directly above the printing bed (Figure 6).

$$\begin{bmatrix} tx' \\ ty' \\ t \end{bmatrix} = \mathbf{M} \begin{bmatrix} x_p \\ y_p \\ 1 \end{bmatrix} = \begin{bmatrix} m_{11} & m_{12} & m_{13} \\ m_{21} & m_{22} & m_{23} \\ m_{31} & m_{32} & m_{33} \end{bmatrix} \cdot \begin{bmatrix} x_p \\ y_p \\ 1 \end{bmatrix} \quad (1)$$

Where  $[x_p \ y_p \ 1]^T$  is the active area of the printed layer,  $\mathbf{M}$  is a projective transformation matrix, and  $[tx' \ ty' \ t]^T$  is the virtual top view.

Each pixel of the virtual top view can be calculated based on the following equation (2):

$$(x', y') = \left( \frac{m_{11}x_p + m_{12}y_p + m_{13}}{m_{31}x_p + m_{32}y_p + m_{33}}, \frac{m_{21}x_p + m_{22}y_p + m_{23}}{m_{31}x_p + m_{32}y_p + m_{33}} \right) \quad (2)$$

It should be noted, however, that the video surveillance area is shifting upwards by the corresponding height with the printing of each new layer, so the unwrapped top view will remain orthogonal to the optical axis of the virtual top camera. Thus, after calculating the vertical shift, the 3D coordinates of the active printing plane  $[X \ Y \ Z \ 1]^T$  are projected onto the image frame to define the 2D boundaries  $[x_p \ y_p \ 1]^T$  for unwrapping (3):

$$\begin{bmatrix} x_p \\ y_p \\ 1 \end{bmatrix} = \mathbf{K} \begin{bmatrix} 1 & 0 & 0 & 0 \\ 0 & 1 & 0 & 0 \\ 0 & 0 & 1 & 0 \end{bmatrix} \begin{bmatrix} \mathbf{R}_{3 \times 3} & \mathbf{t}_{3 \times 1} \\ \mathbf{0}_{1 \times 3} & 1 \end{bmatrix} \begin{bmatrix} X \\ Y \\ Z \\ 1 \end{bmatrix} \quad (3)$$

Where  $[x_p \ y_p \ 1]^T$  is the active area projection onto the image plane,  $\mathbf{K}$  is the intrinsic camera parameters obtained during calibration,  $\mathbf{R}$  is the rotation matrix,  $\mathbf{t}$  is the translation vector, and  $[X \ Y \ Z \ 1]^T$  is the 3D coordinates of the active printing area.

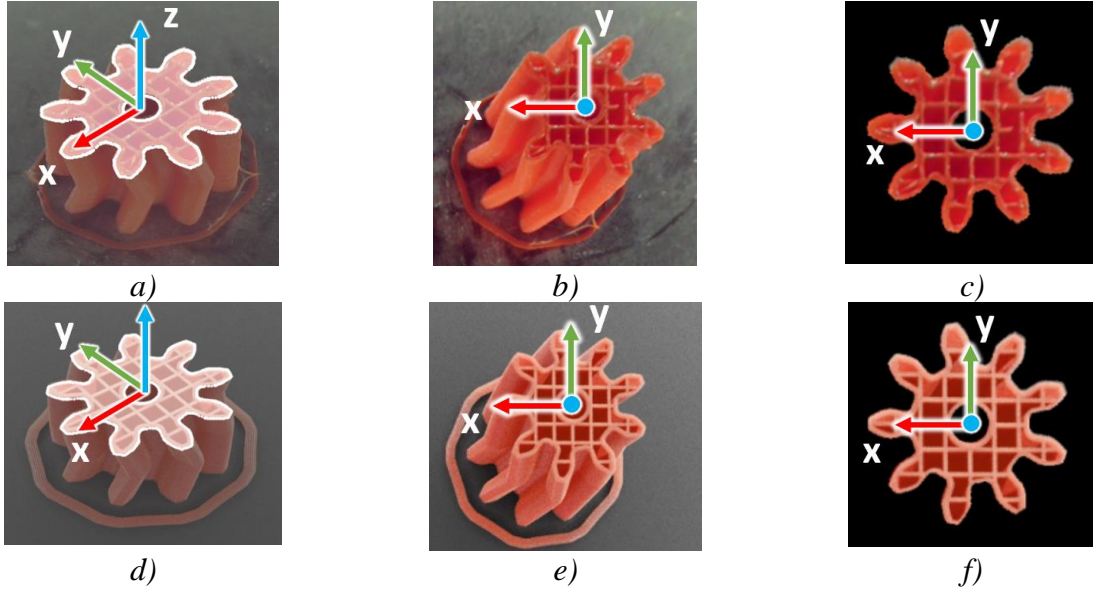


**Figure 6. Virtual top view: a) camera frame, b) unwrapped virtual top view, c) masked printing area, d) Blender scene frame, e) unwrapped synthetic image, f) masked rendered region**

Thus, knowing the camera location and the G-code coordinates, it is possible to rotate the printing area perpendicular to the camera axis, maintaining its origin in the center of the image (Figure 7).

After virtual rotation of the active printing plane, the real image is compared with the reference “ideal” one to analyze its texture and detect any possible defects inside the printed region. Image comparison is based on the similarity degree of the feature descriptors, represented by Histograms of Oriented Gradients (HOG) [64]. The descriptor analyzes local image areas, determines the orientation of the shaded gradients, and expresses this information as a histogram of direction channels.

HOG-based image analysis is widely applied in areas such as pattern recognition, template matching, and similarity determination. For example, Firuzi et al. [65] employed HOG features to recognize defects in electrical transformers, Malik et al. [66] presented a HOG-based landscape similarity analysis, Banerji et al. [67] enhanced HOG features with Fisher Model to extract geo-localization information from large-scale image datasets. Akila and Pavithra [68] developed an object detection algorithm based on scale invariant HOG descriptors, Joshi et al. [69] developed a



sign language recognition system, and Supeng et al. [70] presented a HOG-based template matching algorithm.

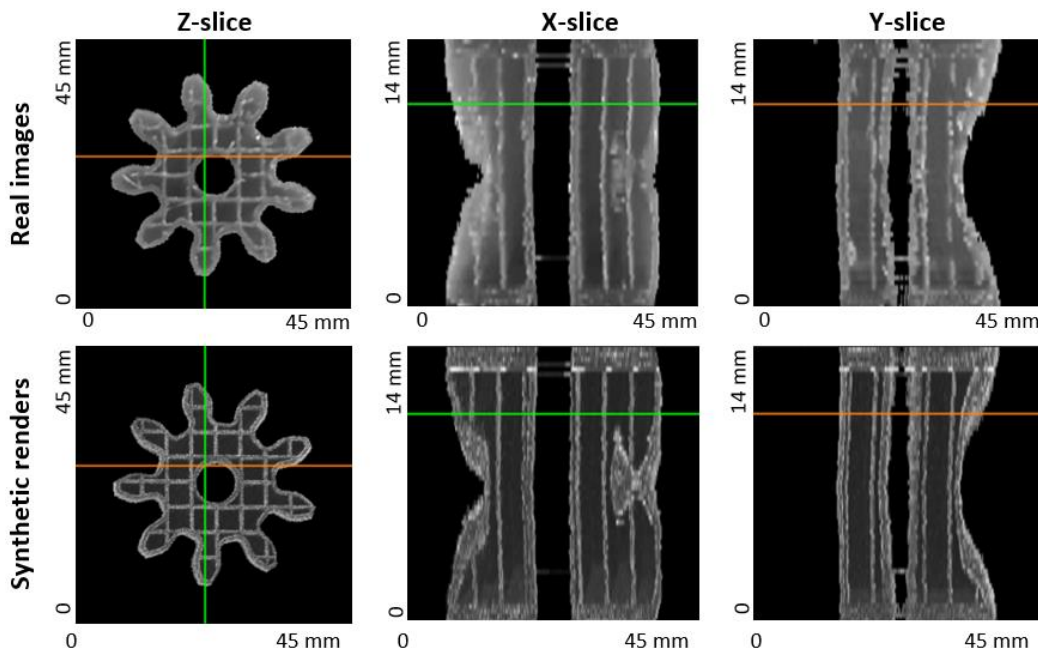


**Figure 7. Consecutive set of unwrapped layers combined into a volumetric view**

Figures 8 and 9 illustrate the detection of the dominant gradient orientation in local image areas and possible characteristic infill patterns with their feature descriptors, respectively. This allows capturing basic geometric structures by detecting the directions of contrasting edges.

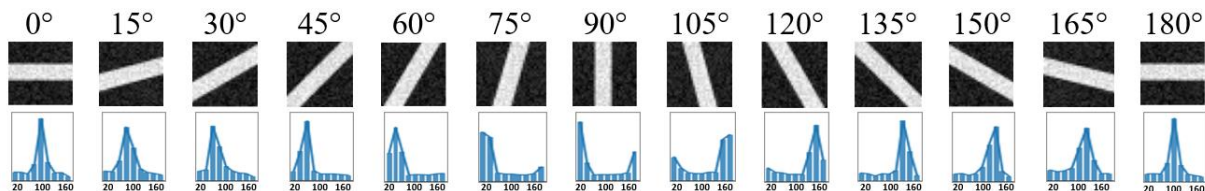


**Figure 8. Detection of the dominant gradient orientation in local image areas (top) using histograms of oriented gradients (bottom)**

As can be seen in Figure 9, changing the direction of light and shadow does not affect the determination of the dominant gradient orientation. The presence of noise, however, lowers the contrast, thereby limiting the capabilities of this method.

Figure 10 shows the stages of comparative image analysis. The image of the printed layer is divided into small sections, square cells, each of which is converted into a feature vector, represented by a nine-channel histogram of oriented gradients, ranging from 0° to 180° with 20-degree intervals. The feature vectors are then combined into normalized 2x2 blocks in such a way that each feature vector simultaneously contributes to several adjacent blocks, which increases the robustness of texture analysis. The same procedure is carried out for the reference synthetic image, after which the obtained histograms are compared. The result of this comparison is expressed in the form of a similarity map, where each section of the original camera image is assigned a

numerical value of the degree of proximity to the “ideal” printing process. These values are then color coded to indicate ideal and non-ideal 3D printing.

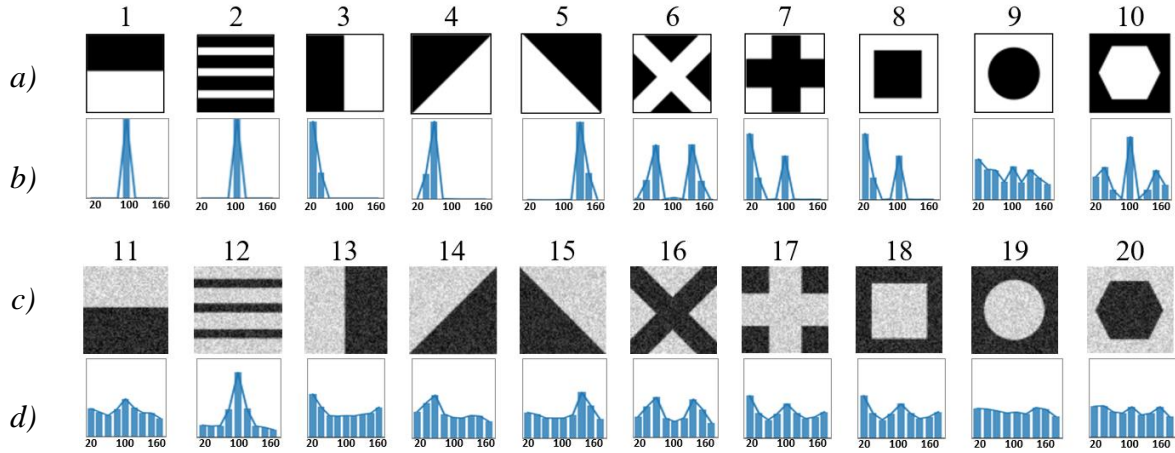


Figure 9. Characteristic infill patterns (a, c) and their feature descriptors (b, d)

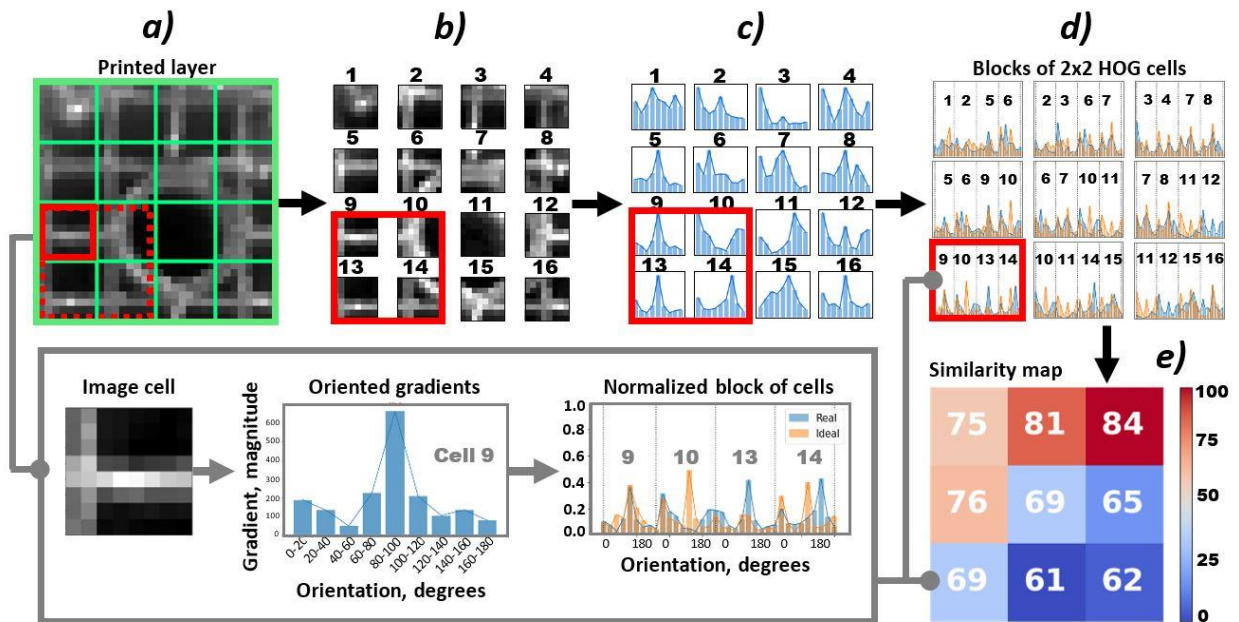


Figure 10. Stages of comparative image analysis: a) splitting the original camera image into local areas, b) separate regions of the source image, c) converting image areas to feature vectors, d) comparison of normalized feature vectors of the original and reference images, e) resulting similarity map

Thus, every unit section of the real image stores unique information from the corresponding area of the printed layer as a collection of features  $\mathbf{p} = [p_1, p_2, \dots, p_k]$ . A single printed layer, in this way, can be represented as a tensor  $\mathbf{F}$  with dimensions  $N \times M \times k$ , where  $N \times M$  is the total number of image blocks, and  $k$  is the number of orientation channels of adjacent block cells. The tensor  $\mathbf{F}$  is then transformed into an  $N \times M$  similarity matrix  $\mathbf{D}$ , each element  $d_{ij}$  of which

represents a similarity function  $f(\mathbf{p}, \mathbf{q})$ , where  $\mathbf{q} = [q_1, q_2, \dots, q_k]$  is a collection of features of the corresponding reference image block.

Comparison of histograms is done by determining the similarity  $s(\mathbf{p}, \mathbf{q})$  between the corresponding vectors,  $\mathbf{p}$  and  $\mathbf{q}$ . A number of similarity metrics were selected based on the comprehensive survey on similarity measures [71], a high-throughput X-ray diffraction pattern analysis [72], and in-depth quantitative analysis in the context of two real problems of image comparison and pattern location [73].

Hernandez–Rivera et al. [72] utilized 49 similarity measures to quantify similarities between Gaussian-based peak responses as a substitute for various characteristics in X-ray diffraction patterns. Research has not found universal metrics for all vector features. It was also found that the behavior of the metric response is not uniform for members of a given similarity family. It was determined, however, that the Clark metric yields a good balance between sensitivity and smooth changes.

Goshtasby et al. [73] found that Pearson correlation coefficient, Spearman’s rho, Kendall’s tau, Jaccard measure,  $L_1$  norm, and squared  $L_2$  norm overall perform better than other measures. Cosine similarity is also widely used in conjunction with HOG features in various pattern recognition tasks [70,74,75].

In this work, the twelve metrics shown in Table 2 were implemented.

**Table 2. Similarity and distance measures**

Metric	Equation	Initial output range	Normalized output range
Cosine similarity	$s(\mathbf{p}, \mathbf{q}) = \frac{\sum p_i q_i}{\sqrt{\sum p_i^2 \sum q_i^2}}$	[1, 0]	[1, 0]
Squared $L_2$ norm	$d(\mathbf{p}, \mathbf{q}) = \sum (p_i - q_i)^2$	[0, 2]	[1, 0]
Pearson’s r	$r(\mathbf{p}, \mathbf{q}) = \frac{\sum (p_i - \mu_p)(q_i - \mu_q)}{\sqrt{\sum (p_i - \mu_p)^2} \cdot \sqrt{\sum (q_i - \mu_q)^2}}$ Where $\mu_p = \frac{1}{n} \sum_{i=1}^n p_i$ and $\mu_q = \frac{1}{n} \sum_{i=1}^n q_i$	[-1, 1]	[1, 0]
Spearman’s rho	$\rho(\mathbf{p}, \mathbf{q}) = 1 - \frac{6 \sum d_i^2}{n(n^2 - 1)}$ Where $d_i$ is the difference between the two ranks of each observation, $n$ is the number of vector elements	[-1, 1]	[1, 0]
Kendall’s tau	$\tau(\mathbf{p}, \mathbf{q}) = \frac{N_c - N_d}{n(n - 1)/2}$	[-1, 1]	[1, 0]

	Where $N_c$ and $N_d$ are the numbers of concordant and discordant pairs of vector elements, respectively		
Jaccard	$s(\mathbf{p}, \mathbf{q}) = \frac{\sum p_i q_i}{\sqrt{\sum(p_i^2 + q_i^2 - p_i q_i)}}$	[1, 0]	[1, 0]
Dice	$s(\mathbf{p}, \mathbf{q}) = \frac{2 \cdot \sum p_i q_i}{\sqrt{\sum(p_i^2 + q_i^2)}}$	[1, 0]	[1, 0]
$L_1$ norm	$d(\mathbf{p}, \mathbf{q}) = \sum  p_i - q_i $	[0, 2]	[1, 0]
Euclidean distance	$d(\mathbf{p}, \mathbf{q}) = \sqrt{\sum (p_i - q_i)^2}$	[0, $\sqrt{2}$ ]	[1, 0]
Hellinger distance	$d(\mathbf{p}, \mathbf{q}) = \sqrt{2 \sum (p_i - q_i)^2}$	[0, 2]	[1, 0]
Sorensen distance	$d(\mathbf{p}, \mathbf{q}) = \frac{\sum  p_i - q_i }{\sum (p_i + q_i)}$	[0, 1]	[1, 0]
Clark distance	$d(\mathbf{p}, \mathbf{q}) = \sqrt{\sum \left( \left  \frac{ p_i - q_i }{p_i + q_i} \right ^2 \right)}$	[0, $\sqrt{2}$ ]	[1, 0]

Similarity metrics  $s(\mathbf{p}, \mathbf{q})$  are expected to satisfy the following properties [73,76]: limited range,  $s \leq s_0$ ; reflexivity,  $s(\mathbf{p}, \mathbf{q}) = s_0$  if  $\mathbf{p} = \mathbf{q}$ ; symmetry,  $s(\mathbf{p}, \mathbf{q}) = s(\mathbf{q}, \mathbf{p})$ , triangle inequality,  $s(\mathbf{p}, \mathbf{q}) \leq s(\mathbf{p}, \mathbf{z}) + s(\mathbf{q}, \mathbf{z})$ , where  $s_0$  is the largest measure between all possible vector inputs.

The input parameters  $\mathbf{p}$  and  $\mathbf{q}$  of the metrics shown in Table 2 are normalized vectors. The output range of similarity values is reduced to [1, 0], where “1” means the identity (overlap) of the input vectors, and “0” means a complete mismatch (no overlap). If a measure represents a distance between two inputs,  $d(\mathbf{p}, \mathbf{q})$ , then the corresponding similarity is determined according to the following equation (4) [72]:

$$s(\mathbf{p}, \mathbf{q}) = 1 - \frac{d(\mathbf{p}, \mathbf{q})}{d^{max}(\mathbf{p}, \mathbf{q})} \quad (4)$$

Where  $d^{max}(\mathbf{p}, \mathbf{q})$  is the absolute maximum possible distance between two input vectors for a particular measure. This method allows comparing all metrics, reducing them to the same scale.

Figure 11 shows the degrees of similarity of various input vectors in the forms of 9-bin histograms, expressed as a percentage of coincidence, reflecting the possible deviations of printed layer sections relative to the reference ones. To achieve maximum efficiency, it is necessary to obtain high similarity values for the first three cases, *a*), *b*), and *c*), and low similarity values for the latter cases, *d*) and *e*). This allows visualizing the efficacy of various similarity measures for specific analytical cases but does not reveal the capabilities of the metrics as applied to real-world problems. From Figure 11, however, it can be concluded that  $L_1$  and  $L_2^2$  norms, as well as Euclidean and Hellinger distances, produce results that are far from expected.

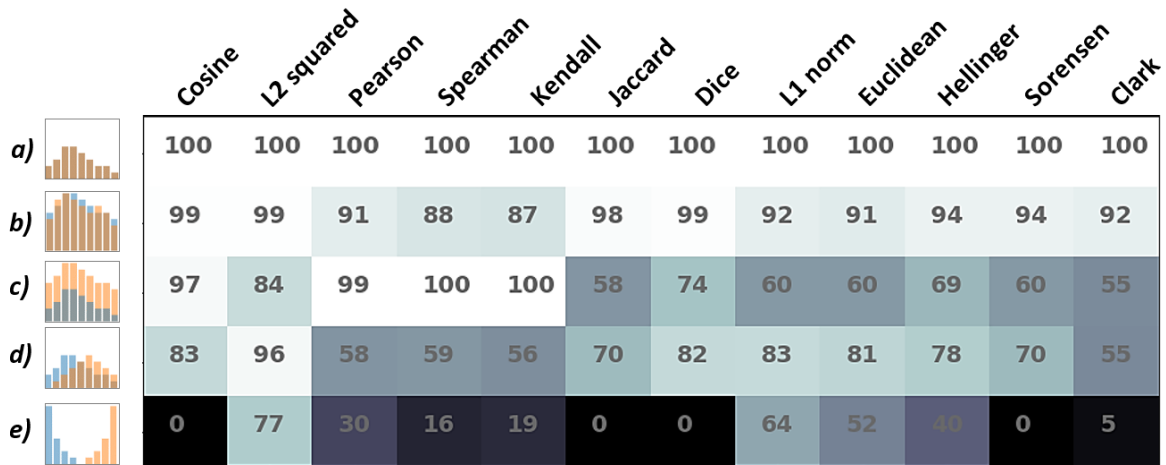


**Figure 11. Normalized similarity measures, expressed as a percentage of coincidence, for the following cases: a) complete match, b) similar histograms with small deviations, c) similar histograms with differences in levels (represents alike image areas with varying illumination parameters), d) histograms with significant shifts, e) non-overlapping histograms**

After the initial assessment of the effectiveness of the selected metrics, Pearson's r, Spearman's rho, Kendall's tau, as well as cosine, Jaccard, Dice, and Sorensen similarities were chosen to test the method for detecting printing errors.

### 3. Results

#### 3.1 Test print modes for selecting optimal similarity measures

To select the optimal similarity metrics, real-life test images were used, reflecting the typical problems of 3D printing. Figure 12 shows the selected test images of erroneous layers for analyzing print mode abnormalities including: a) local infill defects, b) presence of a foreign body in the layer, c) spaghetti problem, d) separation and shift of the printing part from the working surface, e) defects in thin walls, and f) layer shift. A regular printed layer is provided for each failed case, which allows comparing the outputs for various printing regimes and calculating the discriminative power for the selected metrics. In addition to different types of defects, the selected parts have geometries of varying degrees of complexity.

Considering the camera parameters and the size of the working area, the scale of the captured images is 6.67 pixels per millimeter. The size of the minimum area of similarity analysis (2x2 block of 8-pixel cells) is therefore 4.8x4.8 mm, which lies in the range of 5-10% of the entire area of observation. This parameter can potentially be improved by using a high-definition camera.

In addition to continuous similarity for each local area of the image, an experimental failure threshold was also introduced. This is the main criterion for manufacturing defects, which allows varying sensitivity of the selected metrics and unequivocally segmenting the erroneous regions within the printed layers. Thus, an image area is considered defective if its match with the corresponding reference image is less than the chosen threshold.

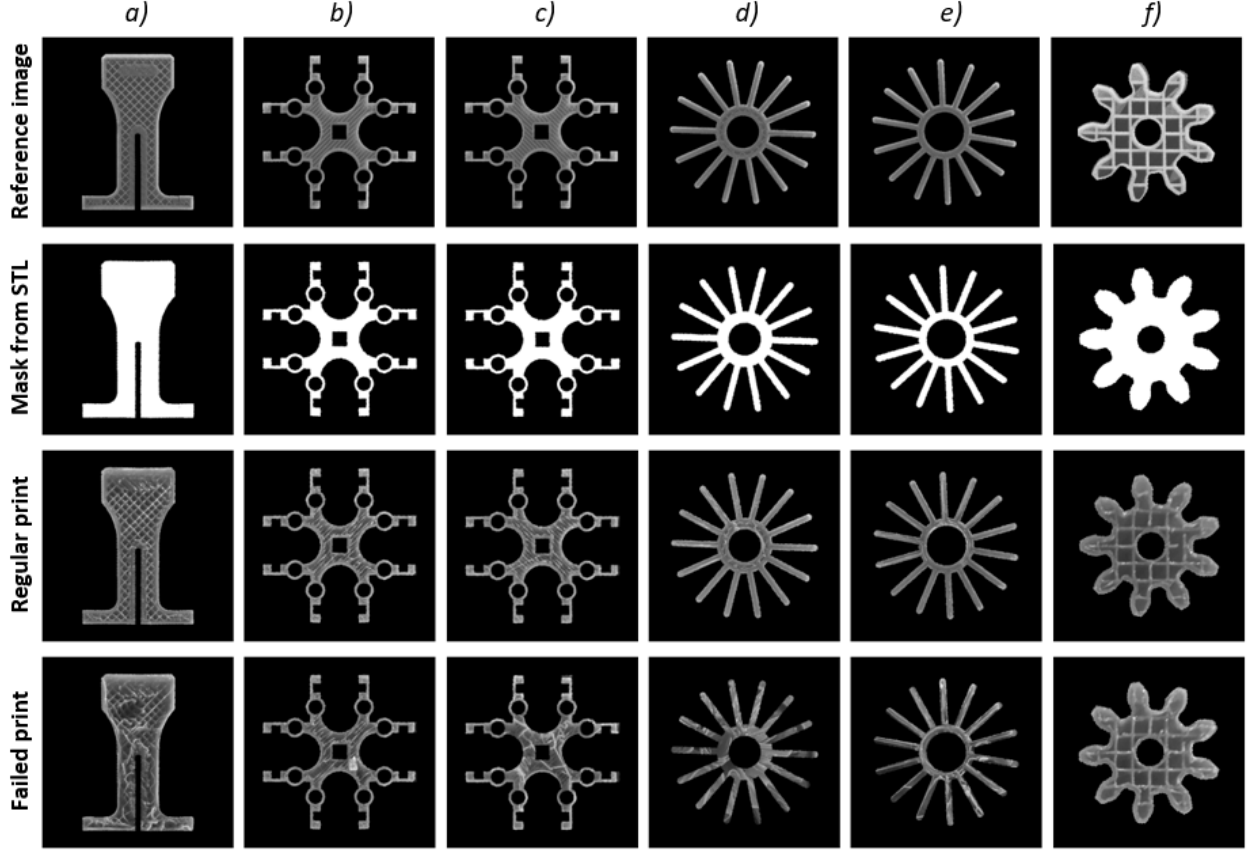


**Figure 12. Test images of regular and failed printed layers: a) local infill defects, b) presence of a foreign body in the layer, c) spaghetti problem, d) separation and shift of the printing part from the working surface, e) defects in thin walls, f) layer shift**

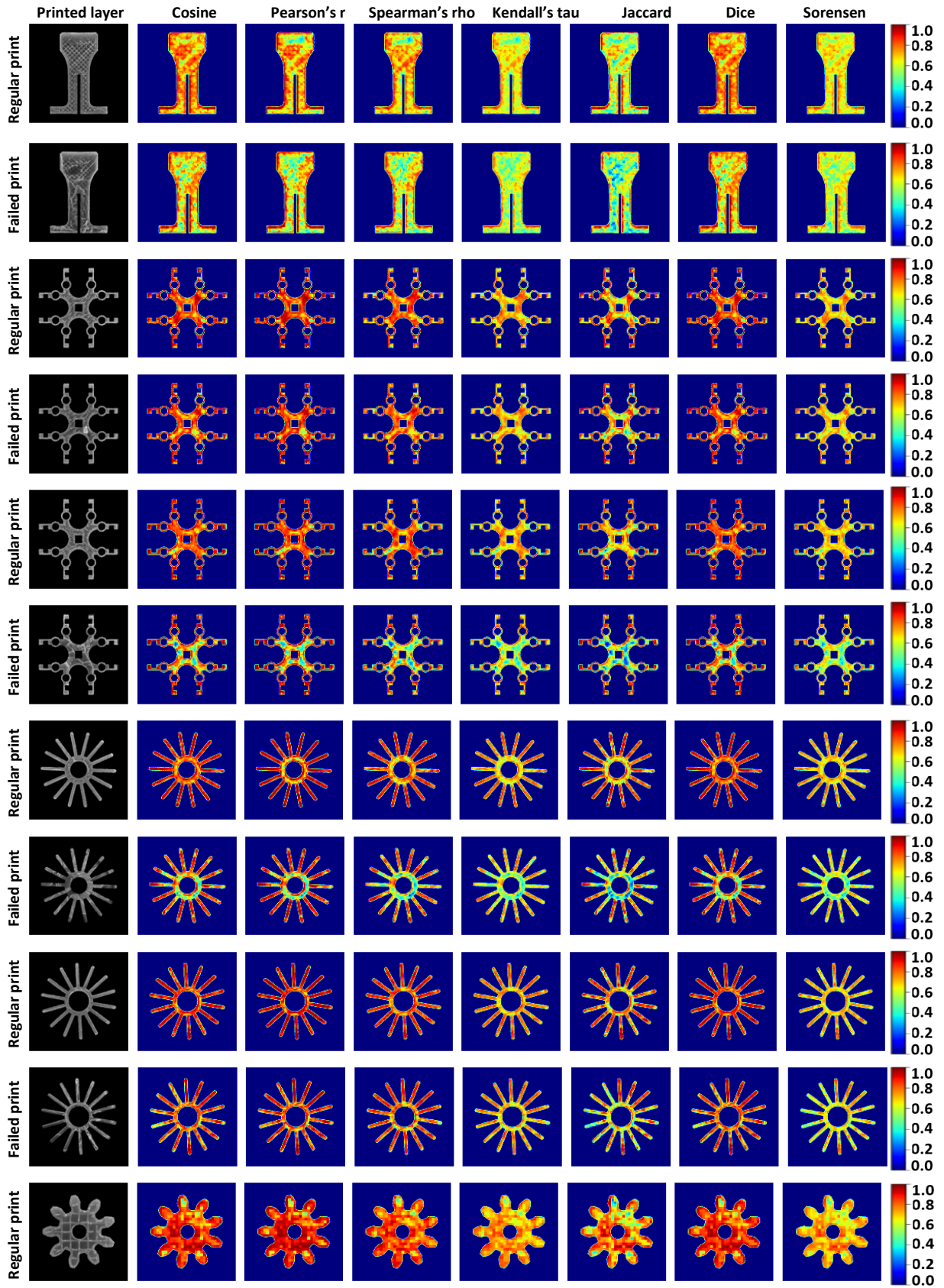
### 3.2 Comparing HOG-based similarity measures

Figure 13 depicts the similarities of test images in the form of heatmaps within the unit range. Each of the metrics can be used to analyze additive manufacturing processes. As can be seen from the heatmaps, Kendall's tau, Jaccard, and Sorensen similarities are the most sensitive, while Pearson's r, Spearman's rho, cosine, and Dice similarities produce more reliable results.

To determine the distinctive power of the selected metrics (Figure 14), an arbitrary 70% failure threshold ( $T_S$ ) was applied to the calculated heatmaps ( $H$ ). A layer region is considered normal if its similarity index is greater than or equal to  $T_S$ . Thus, the overall ratio of anomalous areas ( $a_{\%}$ ) for each layer is calculated using the following expression (5):

$$a_{\%} = \frac{(H \leq T_S)}{S_P} \cdot 100\% \quad (5)$$

Where  $S_P$  is the area of the entire printed layer,  $H$  is the layer similarity, and  $T_S$  is the 70% failure threshold.



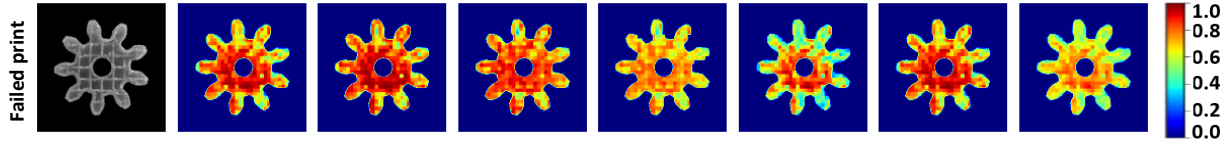


Figure 13. Heat maps of the regular and failed prints for the example components

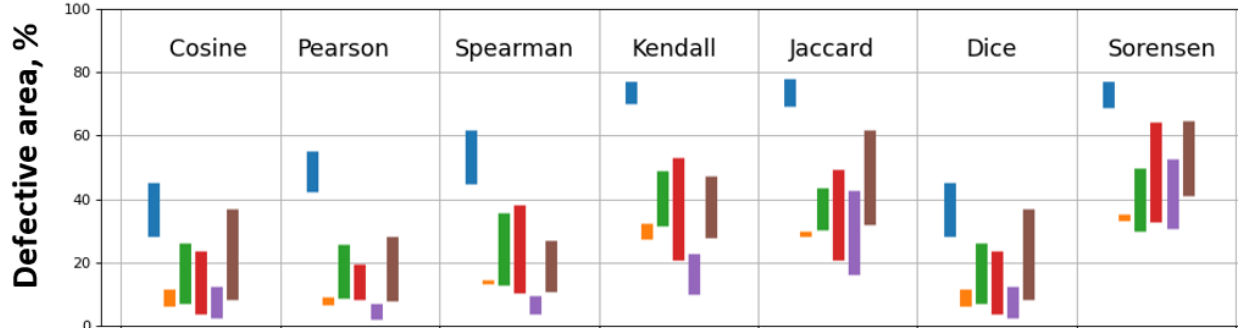


Figure 14. Discriminative power of the selected metrics after applying the 70% failure threshold. Vertical color bars represent the difference between the regular (bottoms) and failed (tops) prints: local infill defects (blue), presence of a foreign body in the layer (orange), spaghetti problem (green), separation and shift of the printing part from the working surface (red), defects in thin walls (purple), layer shift (brown).

Figure 15 shows an example of failure detection and segmentation for the case of cosine similarity.

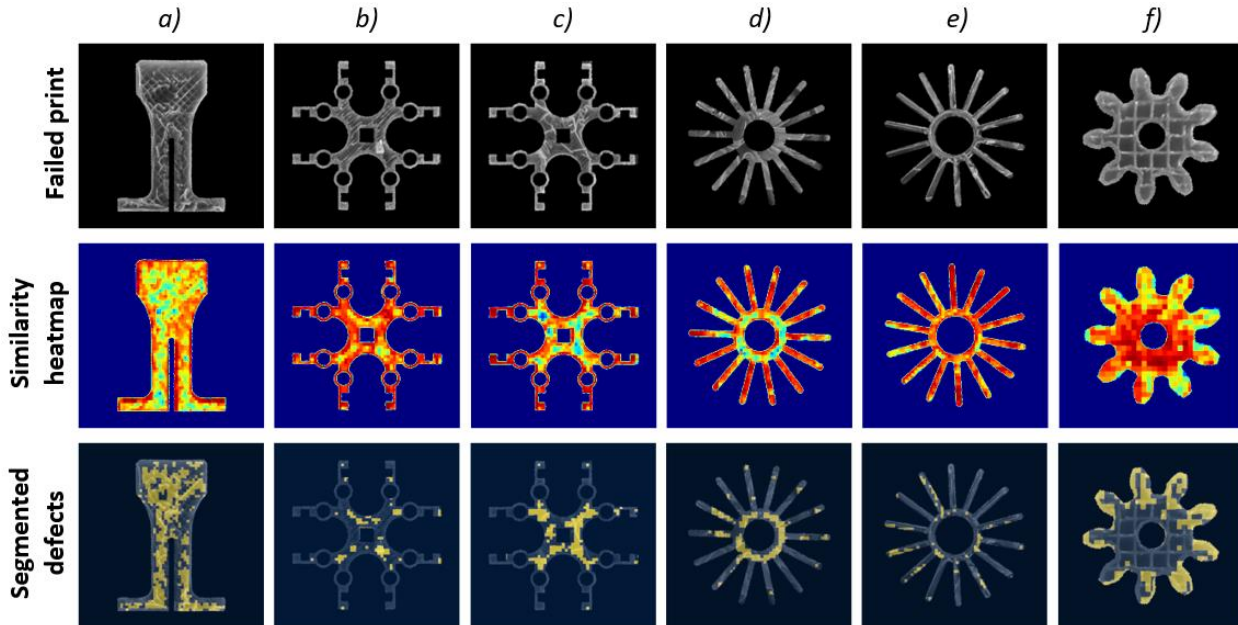


Figure 15. Example of failure detection based on HOG features and cosine similarity: *a)* local infill defects, *b)* presence of a foreign body in the layer, *c)* spaghetti problem, *d)* separation and shift of the printing part from the working surface, *e)* defects in thin walls, *f)* layer shift



#### 4. Discussion

The proposed method makes it possible to analyze 3D printed parts for each layer and segment of anomalous regions with a size of 5 mm or more. The main limiting factor for the developed technique is the time-consuming preliminary rendering. Generating a single image with optimized render settings can take up to several minutes on an Intel Core i7 2.60 GHz system with a dedicated NVIDIA GeForce RTX 2060 GPU. The large size and complex geometric shape of the part increase visualization time. Since the image acquisition and analysis take less than 5 seconds, most of the time spent on in-situ monitoring can be attributed to the pause and nozzle retraction during the image capturing, which can consume more than 20 seconds of time.

There are several previously used approaches to analyze additive manufacturing processes based on information from 3D models (G-code, CAD, or STL) and reference images. Johnson et al. [31] proposed a method using an STL file to generate a binary cross-sectional image of a part corresponding to the layer being inspected. Malik et al. [40] implemented a method for real-time layer-by-layer monitoring of AM processes using G-code-based masking, 3D reconstruction, and augmented reality. Lyngby et al. [77] introduced a real-time vision system for non-nominal AM operation detection employing references from CAD models and color-based image segmentation. Wasserfall et al. [34] proposed a dual camera setup for in-situ layer-wise verification of 3D printed electronics based on known G-code geometry. Hurd et al. [32] presented an approach using a phone camera to validate layers quality by comparing AM process images with 2D images obtained from an STL file. Nuchitprasitchai et al. [30] developed single- and double-camera systems for detecting 5% deviations at every 50th layer utilizing shape and size data from STL files. Delli and Chang [78] proposed a binary 3D printing error detection technique based on support vector machine classification, where the quality check is being performed at critical printing stages based on available images of an ideal printing process. The methods listed above, however, do not employ a physics-based rendering engine and, therefore, do not allow using the rich set of image processing techniques.

The presented method is not limited to the use only in the field of 3D printing. This technique can be applied to compare parts produced by subtractive manufacturing and to reject defective printed circuit boards. The considered rendering system can be suitable for non-expert users to select parameters such as percentage and type of infill, wall thickness, and color of the material at the preprinting stage. Another application is 3D printing in a humanitarian context [79-83] where the work environment has unreliable power supplies or air quality issues such as pollution/debris in the processing environment. This also includes distributed recycling for additive manufacturing (DRAM) [7-10] with non-uniform and heavily contaminated filament. In addition, these methods can also be applied to pellet extrusion 3D printing [84-88] or fused particle fabrication (FPF) [89-93], where particles are direct 3D printed (sometimes as simply shredded waste), as such conditions are more likely to cause critical errors.

The described technique can be applied to FFF 3D printers of all sizes that can be imaged. The additional movable lighting platform used in this work is not necessary equipment since the fundamental factor is the coincidence of physical and virtual printing systems, regardless of lighting conditions. The original 3D model of the physical equipment can be easily customized to

match the actual printing conditions for any type of 3D printer. In the future, the failure detection method can be improved by integrating a physics-based rendering system into the printing process to enable an AI monitored manufacturing process capable of real-time correction of anomalies from digital designs for both AM as well as subtractive manufacturing.

## 5. Conclusions

This study describes the conceptual capabilities of monocular layer-wise in-situ monitoring and analysis of additive manufacturing processes using projective transformations and image processing techniques. The developed method can be applied to material extrusion 3D printers of any size with a resolution of detecting anomalous regions of 5-10% of the overall observation area. The minimum area of similarity analysis can potentially be decreased by using a high-definition camera.

The results show that HOG-based similarity comparison does not introduce significant delays in the monitoring process. The described method, however, requires time resources when preparing the virtual environment and rendering the reference images. Using different similarity metrics and failure thresholds provides flexibility and allows for varying sensitivity in printing anomalies segmentation. Of the twelve similarity and distance measures implemented and compared for their effectiveness at detecting 3D printing errors, the results show that although Kendall's tau, Jaccard, and Sorensen similarities are the most sensitive, Pearson's r, Spearman's rho, cosine, and Dice similarities produce the more reliable results. The greatest efficiency of the given technique can be achieved with the mass production of parts of the same geometric shape as the Blender rendering only needs to occur once. Although this technique was tested here for additive manufacturing, it can be applied to compare parts produced by subtractive manufacturing and printed circuit boards. It can be concluded this method is a promising candidate for enabling smart manufacturing of all kinds in challenging environments such as those for humanitarian 3D printing or distributed recycling for additive manufacturing using complex waste feedstocks.

### **CRedit authorship contribution statement**

**Aliaksei Petsiuk:** Conceptualization, Methodology, Software, Validation, Formal analysis, Investigation, Writing - original draft. **Joshua M. Pearce:** Conceptualization, Methodology, Formal analysis, Resources, Writing - original draft, review & editing, Supervision, Project administration, Funding acquisition.

### **Declaration of Competing Interest**

The authors declare that they have no known competing financial interests or personal relationships that could have appeared to influence the work reported in this paper.

## Acknowledgments

This work was supported by the Witte and Thompson Endowments.

## References

1. E. Sells, S. Bailard, Z. Smith, A. Bowyer, V. Olliver, RepRap: the replicating rapid prototype – maximizing customizability by breeding the means of production, in: F.T. Piller, M.M. Tseng (Eds.), *Handbook of Research in Mass Customization and Personalization*, 1 World Scientific, Singapore, 2009, pp. 568–580.
2. R. Jones, P. Haufe, E. Sells, P. Iravani, V. Olliver, C. Palmer, A. Bowyer, RepRap – the replicating rapid prototype, *Robotica* 29 (1) (2011) 177–191, <https://doi.org/10.1017/S026357471000069X>.
3. A. Bowyer, 3D printing and humanity’s first imperfect replicator, *3D Print. Addit. Manuf.* 1 (1) (2014) 4–5, <https://doi.org/10.1089/3dp.2013.0003>.
4. T.D. Ngo, A. Kashani, G. Imbalzano, K.T.Q. Nguyen, D. Hui, Additive manufacturing (3D printing): A review of materials, methods, applications and challenges, *Composites Part B: Engineering*, 143 (2018), 172–196. <https://doi.org/10.1016/j.compositesb.2018.02.012>.
5. N. Mohan, P. Senthil, S. Vinodh & N. Jayanth, A review on composite materials and process parameters optimisation for the fused deposition modelling process, *Virtual and Physical Prototyping*, 12:1 (2017) 47–59. <https://doi.org/10.1080/17452759.2016.1274490>.
6. R. Anandkumar, S.R. Babu, FDM filaments with unique segmentation since evolution: a critical review. *Prog Addit Manuf* 4 (2019) 185–193. <https://doi.org/10.1007/s40964-018-0069-8>.
7. C. Baechler, M. DeVuono, and J.M. Pearce, Distributed recycling of waste polymer into RepRap feedstock, *Rapid Prototyping Journal*, 19:2 (2013) 118–125. <https://doi.org/10.1108/13552541311302978>.
8. F.A.C. Sanchez, H. Boudaoud, M. Camargo, J.M. Pearce, Plastic recycling in additive manufacturing: A systematic literature review and opportunities for the circular economy. *Journal of Cleaner Production*, 264 (2020), 121602.
9. F.A.C. Sanchez, H. Boudaoud, S. Hoppe, M. Camargo, Polymer recycling in an open-source additive manufacturing context: Mechanical issues. *Additive Manufacturing*, 17 (2017) 87–105.
10. S.C. Dertinger, N. Gallup, N.G. Tanikella, M. Grasso, S. Vahid, P.J. Foot, J.M. Pearce, Technical pathways for distributed recycling of polymer composites for distributed manufacturing: Windshield wiper blades. *Resources, Conservation and Recycling*, 157 (2020), 104810
11. B.T. Wittbrodt, A.G. Glover, J. Laureto, G.C. Anzalone, D. Oppliger, J.L. Irwin, J.M. Pearce, Life-cycle economic analysis of distributed manufacturing with open-source 3-D printers. *Mechatronics*, 23:6 (2013) 713–726.
12. E.E. Petersen, J.M. Pearce, Emergence of home manufacturing in the developed world: Return on investment for open-source 3-D printers. *Technologies*, 5:1 (2017), 7.

13. M. Kreiger, J.M. Pearce, Environmental life cycle analysis of distributed three-dimensional printing and conventional manufacturing of polymer products. *ACS Sustainable Chemistry & Engineering*, 1:12 (2013) 1511-1519.
14. J. Go, S.N. Schiffres, A.G. Stevens, A.J. Hart, Rate limits of additive manufacturing by fused filament fabrication and guidelines for high-throughput system design. *Additive Manufacturing*, 16 (2017) 1-11.
15. H. Wu, Z. Yu, Y. Wang, Experimental study of the process failure diagnosis in additive manufacturing based on acoustic emission. *Measurement*, 136 (2019) 445-453.
16. A. Oleff, B. Küster, M. Stonis, L. Overmeyer, Process monitoring for material extrusion additive manufacturing: a state-of-the-art review. *Prog Addit Manuf* (2021). <https://doi.org/10.1007/s40964-021-00192-4>
17. T. Wohlers, I. Campbell, O. Diegel et al. (2018) Wohlers Report 2018. 3D printing and additive manufacturing state of the industry: Annual Worldwide Progress Report. Wohlers Associates Inc, Fort Collins.
18. M. Borish, B.K. Post, A. Roschli et al., In-situ thermal imaging for single layer build time alteration in large-scale polymer additive manufacturing. *Procedia Manuf* 34 (2019) 482–488. <https://doi.org/10.1016/j.promfg.2019.06.202>.
19. E. Ferraris, J. Zhang, B. van Hooreweder, Thermography based in-process monitoring of Fused Filament Fabrication of polymeric parts. *CIRP Ann Manuf Technol* 68 (2019) 213–216. <https://doi.org/10.1016/j.cirp.2019.04.123>.
20. Y. Tlegenov, G.S. Hong, W.F. Lu, Nozzle condition monitoring in 3D printing. *Robot Comput Integr Manuf* 54 (2018) 45–55. <https://doi.org/10.1016/j.rcim.2018.05.010>.
21. Y. Li, W. Zhao, Q. Li et al., In-situ monitoring and diagnosing for fused filament fabrication process based on vibration sensors. *Sensors* (2019). <https://doi.org/10.3390/s19112589>.
22. P. Becker, C. Roth, A. Roennau et al., Acoustic Anomaly Detection in Additive Manufacturing with Long Short-Term Memory Neural Networks. *IEEE 7th Int Conf Ind Eng Appl (ICIEA)* (2020) 921–926. <https://doi.org/10.1109/ICIEA49774.2020.9102002>.
23. F. Li, Z. Yu, Z. Yang et al., Real-time distortion monitoring during fused deposition modeling via acoustic emission. *Struct Health Monit* 19 (2019) 412–423. <https://doi.org/10.1177/1475921719849700>.
24. D.D.L. Chung, S. Somaratna, Laboratory simulation of capacitance-based layer-by-layer monitoring of three-dimensional printing. *Sens Actuators A Phys* 268 (2017) 101–109. <https://doi.org/10.1016/j.sna.2017.10.061>.
25. Y. Tlegenov Y, W.F. Lu, G.S. Hong, A dynamic model for current-based nozzle condition monitoring in fused deposition modelling. *Prog Addit Manuf* 4 (2019) 211–223. <https://doi.org/10.1007/s40964-019-00089-3>.
26. R.K. Rao, J. Liu, D. Roberson et al., Online Real-Time Quality Monitoring in Additive Manufacturing Processes Using Heterogeneous Sensors. *J Manuf Sci Eng* (2015). <https://doi.org/10.1115/1.4029823>.
27. E.C. Koskelo, E.B. Flynn, P.J. Shull, A.L. Gyekenyesi, T. Yu, H.F. Wu, Scanning laser ultrasound and wavenumber spectroscopy for in-process inspection of additively manufactured parts. *Proc SPIE Nondestruct Charact Monit Adv Mater Aerosp Civ Infrastruct* (2016). <https://doi.org/10.1117/12.2222130>.

28. T.J. Coogan, D.O. Kazmer, In-line rheological monitoring of fused deposition modeling. *J Rheol* 63 (2019) 141–155. <https://doi.org/10.1122/1.5054648>.
29. J. Li, H. Xie, K. Ma, In-situ monitoring of the deformation during Fused Deposition Modeling process using CGS method. *Polym Test* 76 (2019) 166–172. <https://doi.org/10.1016/j.polymertesting.2019.03.030>.
30. S. Nuchitprasitchai, M.C. Roggemann, J.M. Pearce, Factors effecting real-time optical monitoring of fused filament 3D printing, *Prog. Addit. Manuf. J.* 2 (3) (2017) 133–149, <https://doi.org/10.1007/s40964-017-0027-x> 2017.
31. A. Johnson, H. Zarezadeh, X. Han, R. Bibb, R. Harris, Establishing in-process inspection requirements for material extrusion additive manufacturing. Loughborough University. Conference contribution (2016). <https://hdl.handle.net/2134/20696>.
32. S. Hurd, C. Camp, J. White, Quality assurance in additive manufacturing through mobile computing. *Int Conf Mob Comput Appl Serv* (2015) 203–220. [https://doi.org/10.1007/978-3-319-29003-4\\_12](https://doi.org/10.1007/978-3-319-29003-4_12).
33. H. Jeong, M. Kim, B. Park et al., Vision-Based Real-Time Layer Error Quantification for Additive Manufacturing. *Proc ASME 2017 12th Int Manuf Sci Eng Conf.* (2017). <https://doi.org/10.1115/MSEC2017-2991>.
34. F. Wasserfall, D. Ahlers, N. Hendrich, Optical in-situ verification of 3D-printed electronic circuits. *IEEE 15th Int Conf Autom Sci and Eng (CASE)* (2019). <https://doi.org/10.1109/COASE.2019.8842835>.
35. A. Ceruti, A. Liverani, T. Bombardi, Augmented vision and interactive monitoring in 3D printing process. *Int J Interact Des Manuf* 11 (2017) 385–395. <https://doi.org/10.1007/s12008-016-0347-y>.
36. J. Straub, 3D printing cybersecurity: Detecting and preventing attacks that seek to weaken a printed object by changing fill level. *Proc SPIE Dimens Opt Metrol Insp Pract Appl VI* (2017). <https://doi.org/10.1117/12.2264575>.
37. M.D. Kutzer, L.D. DeVries, C.D. Blas, Part monitoring and quality assessment of conformal additive manufacturing using image reconstruction. *Proc ASME 2018 Int Des Eng Tech Conf Comput Inf Eng Conf 5B* (2018). <https://doi.org/10.1115/DETC2018-85370>
38. Z. Chen, R. Horowitz, Vision-assisted arm motion planning for freeform 3D Printing. *2019 Am Control Conf (ACC)* (2019) 4204–4209. <https://doi.org/10.23919/ACC.2019.8814699>.
39. H. Shen, W. Du, W. Sun et al., Visual detection of surface defects based on self-feature comparison in robot 3-D printing. *Appl Sci.* (2020). <https://doi.org/10.3390/app10010235>.
40. A. Malik, H. Lhachemi, J. Ploennigs et al., An application of 3D model reconstruction and augmented reality for real-time monitoring of additive manufacturing. *Procedia CIRP* 81 (2019) 346–351. <https://doi.org/10.1016/j.procir.2019.03.060>.
41. A.L. Petsiuk, J.M. Pearce. Open source computer vision-based layer-wise 3D printing analysis. *Additive Manufacturing* 36 (2020), 101473. <https://doi.org/10.1016/j.addma.2020.101473>.

42. G.C. Anzalone, B. Wijnen, J.M. Pearce, Multi-material additive and subtractive prosumer digital fabrication with a free and open-source convertible delta RepRap 3-D printer, *Rapid Prototyp. J.* 21 (5) (2015) 506–519, <https://doi.org/10.1108/RPJ-09-2014-0113>.
43. RAMPS 1.4. [https://reprap.org/wiki/RAMPS\\_1.4](https://reprap.org/wiki/RAMPS_1.4), 2021 (accessed 03 November 2021).
44. SONY IMX322 Datasheet. [https://dashcamtalk.com/cams/lk-7950-wd/Sony\\_IMX322.pdf](https://dashcamtalk.com/cams/lk-7950-wd/Sony_IMX322.pdf), 2021 (accessed 03 November 2021),
45. Blender, free and open source 3D creation suite. <https://www.blender.org/>, 2021 (accessed 03 November 2021).
46. B.R. Kent. Visualizing Astronomical Data with Blender. *PASP* 125:928 (2013) 731. <https://iopscience.iop.org/article/10.1086/671412/meta>.
47. M. Gschwandtner, R. Kwitt, A. Uhl, W. Pree, BlenSor: Blender Sensor Simulation Toolbox. In: Bebis G. et al. (eds) *Advances in Visual Computing. ISVC 2011. Lecture Notes in Computer Science*, 6939 (2011). Springer, Berlin, Heidelberg. [https://doi.org/10.1007/978-3-642-24031-7\\_20](https://doi.org/10.1007/978-3-642-24031-7_20).
48. R.F. da Costa, D.S. de Medeiros, R. Andrade, O. Saotome, and R. Machado. General Purpose Radar Simulator based on Blender Cycles Path Tracer. (2020). DOI: 10.14209/SBRT.2020.1570649487.
49. S. Flaischlen, G.D. Wehinger, Synthetic Packed-Bed Generation for CFD Simulations: Blender vs. STAR-CCM+. *ChemEngineering*, 3(2) (2019) 52. <https://doi.org/10.3390/chemengineering3020052>.
50. M. Ilba, Estimating the daily solar irradiation on building roofs and facades using Blender Cycles path tracing algorithm. *E3S Web of Conferences* 10, 00027 (2016) <https://doi.org/10.1051/e3sconf/20161000027>.
51. D.P. Rohe, An Optical Test Simulator Based on the Open-Source Blender Software. United States: N. p., 2019. Web. <https://www.osti.gov/biblio/1642949>.
52. S. Reitmann, L. Neumann, B. Jung, BLAINDER—A Blender AI Add-On for Generation of Semantically Labeled Depth-Sensing Data. *Sensors*. 2021; 21(6):2144. <https://doi.org/10.3390/s21062144>.
53. Blender: Procedural Textures. [https://docs.blender.org/manual/en/2.79/render/blender\\_render/textures/types/procedural/index.html](https://docs.blender.org/manual/en/2.79/render/blender_render/textures/types/procedural/index.html), 2021 (accessed 03 November 2021).
54. Chris Bailey. Top 6 Blender Nodes To Make Any Material in Blender 2021. <https://www.youtube.com/watch?v=yffWd4kI51Q>, 2021 (accessed 03 November 2021).
55. Blender Shader Nodes. <https://docs.blender.org/manual/en/2.79/render/cycles/nodes/types/shaders/index.html>, 2021 (accessed 03 November 2021).
56. Heinz Löpmeier, Blender-Gcode-Importer. <https://github.com/Heinz-Loepmeier/Blender-Gcode-Import>, 2021 (accessed 03 November 2021).
57. Jonathan Winterflood, YAGV - Yet Another Gcode Viewer, v0.4. <https://github.com/jonathanwin/yagv>, 2021 (accessed 03 November 2021).
58. Alessandro Zomparelli, Gcode Exporter. <https://github.com/alessandro-zomparelli/gcode-exporter>, 2021 (accessed 03 November 2021).
59. Blender for Science, Gcode Exporter. <https://github.com/blender-for-science/import-G-code>, 2021 (accessed 03 November 2021).

60. Petsiuk, A., & Pearce, J. M. (2021, October 25). Layer-wise HOG-based anomaly detection in plastic FFF 3D printing. Retrieved from <https://osf.io/q8ebj/>, 2021 (accessed 03 November 2021)..
61. Blender Cycles, <https://docs.blender.org/manual/en/latest/render/cycles/index.html>, 2021 (accessed 03 November 2021).
62. OpenCV: Camera Calibration and 3D Reconstruction. [https://docs.opencv.org/3.4/d9/d0c/group\\_calib3d.html](https://docs.opencv.org/3.4/d9/d0c/group_calib3d.html), 2021 (accessed 03 November 2021).
63. OpenCV: Geometric Image Transformations. [https://docs.opencv.org/4.5.2/da/d54/group\\_imgproc\\_transform.html](https://docs.opencv.org/4.5.2/da/d54/group_imgproc_transform.html), 2021 (accessed 03 November 2021).
64. N. Dalal and B. Triggs, Histograms of oriented gradients for human detection, 2005 IEEE Computer Society Conference on Computer Vision and Pattern Recognition (CVPR'05), 2005, pp. 886-893 vol. 1, doi: 10.1109/CVPR.2005.177.
65. Firuzi, M. Vakilian, B. T. Phung and T. R. Blackburn, Partial Discharges Pattern Recognition of Transformer Defect Model by LBP & HOG Features, in *IEEE Transactions on Power Delivery*, vol. 34, no. 2, pp. 542-550, April 2019, doi:10.1109/TPWRD.2018.2872820.
66. K. Malik, C. Robertson, Landscape Similarity Analysis Using Texture Encoded Deep-Learning Features on Unclassified Remote Sensing Imagery. *Remote Sensing*, 13:3 (2021) 492. <https://doi.org/10.3390/rs13030492>.
67. S. Banerji et al. Finding Better Matches: Improving Image Retrieval with EFM-HOG, *International Journal on Advances in Software*, 13:3-4 (2020). [http://math.lakeforest.edu/banerji/research\\_files/IJAS.pdf](http://math.lakeforest.edu/banerji/research_files/IJAS.pdf),
68. K. Akila and P. Pavithra. Optimized Scale Invariant HOG Descriptors for Object and Human Detection, *IOP Conf. Ser.: Mater. Sci. Eng.* (2021) **1119** 012002.
69. G. Joshi, S. Singh, R. Vig, Taguchi-TOPSIS based HOG parameter selection for complex background sign language recognition, *Journal of Visual Communication and Image Representation*, 71 (2020), 102834, <https://doi.org/10.1016/j.jvcir.2020.102834>.
70. J. Supeng, X. Wei, Y. Liu, Robust template matching algorithm with multi-feature using best-buddies similarity. *Proceedings*, v.11427 (2020), Second Target Recognition and Artificial Intelligence Summit Forum; 114271Y (2020). <https://doi.org/10.1117/12.2552038>.
71. S.H. Cha, Comprehensive survey on distance/similarity measures between probability density functions, *Int. J. Math. Model. Meth. Appl. Sci.* (2007) 1.
72. E. Hernandez-Rivera, S.P. Coleman, M.A. Tschopp, Using similarity metrics to quantify differences in high-throughput datasets: application to X-ray diffraction patterns, *ACS Comb. Sci.* 19 (1) (2016) 25–36, <https://doi.org/10.1021/acscombsci.6b00142>.
73. A.A. Goshtasby, Similarity and dissimilarity measures, in: S. Singh, S.B. Kang (Eds.), *Image Registration. Advances in Computer Vision and Pattern Recognition*, Ch. 2, Springer, London, United Kingdom, 2012, pp. 7–66, , [https://doi.org/10.1007/978-1-4471-2458-0\\_2](https://doi.org/10.1007/978-1-4471-2458-0_2).
74. R. K. Sharma, N. Tater and R. Kumar, Genuinity Detection of People: A Comparative Analysis on HOG and One Shot Learning, *2020 6th International Conference on Signal*

- Processing and Communication (ICSC)*, 2020, pp. 167-172, doi: 10.1109/ICSC48311.2020.9182738.
75. J. Chen, Z. Guo, J. Hu, Ring-Regularized Cosine Similarity Learning for Fine-Grained Face Verification, *Pattern Recognition Letters*, 148 (2021) 68-74. <https://doi.org/10.1016/j.patrec.2021.04.029>.
  76. S. Theodoridis, K. Koutroumbas, *Pattern Recognition*, 4th edn. Academic Press, New York (2009), pp. 602, 605, 606.
  77. R.A. Lyngby, J. Wilm, E.R. Eiríksson et al., In-line 3D print failure detection using computer vision. Joint Special Interest Group meeting between euspen and ASPE: Dimensional Accuracy and Surface Finish in Additive Manufacturing (2017). <https://www.euspen.eu/knowledge-base/AM17133.pdf>.
  78. U. Delli, S. Chang, Automated processes monitoring in 3D printing using supervised machine learning, *Procedia Manuf.* 26 (2018) 865–870, <https://doi.org/10.1016/j.promfg.2018.07.111>.
  79. L. Corsini, C.B. Aranda-Jan, J. Moultrie, The impact of 3D printing on the humanitarian supply chain. *Production Planning & Control* (2020) 1-13.
  80. O. Rodríguez-Espíndola, S. Chowdhury, A. Beltagui, and P. Albores, The potential of emergent disruptive technologies for humanitarian supply chains: the integration of blockchain, Artificial Intelligence and 3D printing. *International Journal of Production Research*, 58:15 (2020) 4610-4630.
  81. B.L. Savonen, T.J. Mahan, M.W. Curtis, J.W. Schreier, J.K. Gershenson, and J.M. Pearce, Development of a resilient 3-D printer for humanitarian crisis response. *Technologies*, 6:1 (2018) 30.
  82. J. Loy, P. Tatham, R. Healey, and C.L. Tapper, 2016. 3D Printing Meets Humanitarian Design Research: Creative Technologies in Remote Regions. In *Creative Technologies for Multidisciplinary Applications* (pp. 54-75). IGI Global.
  83. S. Lipsky, A. Przyjemski, M. Velasquez, and J. Gershenson, 2019, October. 3D Printing for Humanitarian Relief: The Printer Problem. In *2019 IEEE Global Humanitarian Technology Conference (GHTC)* (pp. 1-7). IEEE.
  84. S. Whyman, K.M. Arif, and J. Potgieter, 2018. Design and development of an extrusion system for 3D printing biopolymer pellets. *The International Journal of Advanced Manufacturing Technology*, 96(9-12), pp.3417-3428.
  85. S. Singamneni, D. Smith, M.J. LeGuen, and D. Truong, Extrusion 3D printing of polybutyrate-adipate-terephthalate-polymer composites in the pellet form. *Polymers*, 10:8 (2018) 922.
  86. T. Cersoli, A. Cresanto, C. Herberger, E. MacDonald, and P. Cortes, 3D printed shape memory polymers produced via direct pellet extrusion. *Micromachines*, 12:1 (2021) 87.
  87. S. Singamneni, A. Warnakula, D.A. Smith, and M.J. Le Guen, Biopolymer alternatives in pellet form for 3D printing by extrusion. *3D Printing and Additive Manufacturing*, 6:4 (2019) 217-226.
  88. D.M. Nieto, V.C. López, and S.I. Molina, Large-format polymeric pellet-based additive manufacturing for the naval industry. *Additive Manufacturing*, 23 (2018) 79-85.



89. A.L. Woern, D.J. Byard, R.B. Oakley, M.J. Fiedler, S.L. Snabes, and J.M. Pearce, Fused particle fabrication 3-D printing: Recycled materials' optimization and mechanical properties. *Materials*, 11:8 (2018) 1413.
90. M.J. Reich, A.L. Woern, N.G. Tanikella, and J.M. Pearce, Mechanical properties and applications of recycled polycarbonate particle material extrusion-based additive manufacturing. *Materials*, 12:10 (2019) 1642.
91. A. Alexandre, F.A. Cruz Sanchez, H. Boudaoud, M. Camargo, and J.M. Pearce, Mechanical properties of direct waste printing of polylactic acid with universal pellets extruder: comparison to fused filament fabrication on open-source desktop three-dimensional printers. *3D Printing and Additive Manufacturing*, 7:5 (2020) 237-247.
92. D.J. Byard, A.L. Woern, R.B. Oakley, M.J. Fiedler, S.L. Snabes, and J.M. Pearce, Green fab lab applications of large-area waste polymer-based additive manufacturing. *Additive Manufacturing*, 27 (2019) 515-525.
93. H.A. Little, N.G. Tanikella, M.J. Reich, M.J. Fiedler, S.L. Snabes, and J.M. Pearce, Towards distributed recycling with additive manufacturing of PET flake feedstocks. *Materials*, 13:19 (2020) 4273.